Journal of Electroanalytical Chemistry 935 (2023) 117353

Contents lists available at ScienceDirect

Journal of Electroanalytical Chemistry

journal homepage: www.elsevier.com/locate/jelechem

Applying CeO_2 nanorods in flexible electrochemical immunosensor to detect C-reactive protein

Rafael Aparecido Ciola Amoresi [a,b,*], Noemí Angélica Vieira Roza [c], Talita Mazon [c]

[a] School of Engineering, São Paulo State University – UNESP, Guaratinguetá, 12516-410, São Paulo, Brazil
[b] Center for Engineering, Modeling and Applied Social Sciences, Federal University of ABC, Dos Estados Avenue, 5001, 09210-580 Santo André, SP, Brazil
[c] Center for Information Technology Renato Archer, CTI, Rod. D. Pedro I, KM 143.6, 13069-901 Campinas, SP, Brazil

ARTICLE INFO

Keywords:
Immunosensor
CRP
CeO_2
Nanoparticles

ABSTRACT

In this work, we report the development of a flexible electrochemical immunosensor based on CeO_2 nanorods (NRs) immobilized with C-reactive protein (CRP) antibody, a biomarker of cardiovascular disease. CeO_2 NRs were obtained by microwave-assisted hydrothermal method and characterized by XRD, TEM, and XPS. For the preparation of the working electrode, WE, of the immunosensor, the NRs were dispersed in organic solvent and then functionalized with cystamine and glutaraldehyde, and then modified with CRP antibody. The deposition condition was evaluated for electrode functionalization and immobilization. Functionalization and immobilization were verified by spectroscopic techniques and proved effective repeatability and reproducibility. The developed immunosensor had acceptable reproducibility (coefficient of variation = 4.5 %), allowed detection in the range of 0.3 to 7.0 mg L^{-1} of CRP with a detection limit of 0.18 mg L^{-1}, and applications that are immediately detectable, easy-to-handle, low-cost and ideal for point-of-care.

1. Introduction

C-reactive protein (CRP) is a ring-shaped, pentameric protein synthesized by the liver and whose level increases in response to inflammation. The name came about because it was first identified as a substance present in the plasma of patients during the acute phase of pneumococcal pneumonia, in which it reacted with pneumococcal C-polysaccharide [1,2]. Elevated CRP levels result from a number of causes, which include acute and chronic conditions, in which markedly elevated levels are most often associated with an infectious cause [3]. The concentration of CRP in healthy individuals is 0.8 mg L^{-1}, however, can rapidly increase to over 1000 times normal after tissue injury, infection or inflammation [2,4]. Furthermore, the increase in CRP levels in patients with hypertension predicts the development of heart failure, which may indicate that CRP itself has a pathogenic role in cardiac remodeling [4,5]. There are disagreements about the direct or indirect role of CRP in diseases related to heart failure [6,7], however, the existing results suggest a correlation between plasma CRP and the degree of coronary atherosclerosis [8]. Therefore, the continued development of accurate and rapid analytical methods for the detection of CRP is imperative.

Regarding the methods for CRP detection, there is the ELISA (Enzyme-linked immunosorbent assay) [9] in which is the most popular and with a detection capacity of 1 mg L^{-1}, however, this method has disadvantages either the prolonged time required for detection as the relatively high false results rate due to non-specific bindings [10]. Other detection methods for CRP are dedicated to the construction of biosensors such as those based on piezoelectric biosensors [11], with nanoparticles loaded on derived nanoporous carbons [12], or surface plasmon resonance (SPR)-based systems [13]. However, the most required and advantageous biosensor devices currently are those which allow chemical modifications of the electrode surface and at the same time are flexible, disposable, inexpensive, and reproducible [14,15].

In this sense, electrochemical analysis is presented as a method of real time operation, thus it is of fast detection, in addition to presenting characteristics of sensitivity and easy to manufacture on different surfaces, allowing the obtainment of biosensors on flexible, portable, and miniaturized electrodes [16]. The most recent works based on immunosensors for detection of CRP demonstrate good results of limit and range of detection [12,17,18], however, they are either built on electrodes based on glassy carbon or they use oxidant agents such as

* Corresponding author.
E-mail addresses: ciola.amoresi@ufabc.edu.br, rafaelciola@yahoo.com.br (R.A.C. Amoresi).

https://doi.org/10.1016/j.jelechem.2023.117353
Received 9 November 2022; Received in revised form 9 March 2023; Accepted 16 March 2023
Available online 20 March 2023

hydrogen peroxide, in which such factors are unfavorable to the application of point-of-care tests (POCT).

For this reason, in this work we built a portable, easy-to-use, low-cost biosensor on a flexible electrode, which enhances its application for diagnosis at the point-of-care as well as research as a wearable biosensor [19]. The research is dedicated to optimizing the bioreceptor, that is, the immobilized sensitive biological element that recognizes the analyte, ensuring its stability and high-sensitivity in a short response time, with high reproducibility.

In this perspective, nanoparticulate oxides are advantageous materials for the immobilization of biological elements since they present high biocompatibility [20], due to the ease of surface interaction, either by electrostatic adsorption or chemical interaction by covalent bonds of amine groups and residual cysteine present in biomolecules [21,22], resulting in immobilization. Cerium oxide nanoparticles are strong candidates for application as surfaces susceptible to the immobilization of biomolecules. The physicochemical characteristics of this oxide are the cubic crystal structure, semiconductivity with band gap energy at ~ 3.2 eV, it has a high oxygen storage capacity and allows easy mobility of vacancies due to the ability to convert the Ce^{4+} and Ce^{3+} oxidation states [23,24].

The CeO_2 different morphologies nanoparticles show influence on the surface properties of this oxide. It is observed that nanorod-like, NRs (a 2D material), morphologies present high charge density [25] and higher surface reactivity [26] compared to other morphologies. Another important factor for the adsorption and surface reactivity characteristics is the isoelectric point, IEP, in which CeO_2 has a high IEP, with a value of 9.2 [27]. IEP is the pH value that results in zero net charge on the surface of a material, high difference in the IEP value between the adsorbent and the adsorbate is often a factor that indicates better adsorption characteristics [28]. In this context, this is verified for the molecule that will act as an adsorbate, the CRP molecule, which has an IEP of 5.3 [29]. In addition, several surface applications such as catalytic [30], photocatalytic [31], and sensor [32,33] are verified for CeO_2, indicating it as a material with peculiar surface characteristics [34]. However, for applications as a biosensor this material has been little explored [35].

Therefore, in this work we are evaluating the application of CeO_2 with nanorod morphology, as a flexible electrode immunosensor, using a simple methodology, with few steps in the antibody immobilization and a low number of biological reagents compared to other works [36]. The evaluated of the conditions of deposition of the CeO_2 NRs on the working electrode (WE) is performed using dimethylformamide (DMF) and glutaraldehyde (Gluta) as dispersants. The effective functionalization of CeO_2 NRs with cystamine (Cys) and Gluta, and subsequent immobilization with anti-CRP, was demonstrated and discussed. Finally, different concentrations of CRP antigen were tested on the immobilized electrode, showing that the developed immunosensor resulted levels of limit of detection for CRP used in clinical trials.

2. Experimental

2.1. CeO_2 NRs synthesis and characterization

CeO_2 NRs were obtained using the microwave assisted hydrothermal (MAH) method. Cerium nitrate hexahydrate ($Ce(NO)_3{\cdot}6H_2O$, 99 %, Neon) and sodium hydroxide (NaOH, 97 %, Neon) were used. The cerium salt was dissolved in a NaOH solution (6 mol L^{-1}) and stirred for 1 h at 25 °C. Then the suspension was transferred to the MAH system (180 °C / 8 min). The precipitate obtained was collected at room temperature and washed with deionized water until reaching neutral pH. The powder was dried in an oven at 70°/12 h. The CeO_2 NRs were characterized via X-ray diffractogram (XRD) patterns using a D/Max-2000PC diffractometer, Rigaku (Japan), with Cu Kα radiation (λ = 1.5406 Å) in the 2θ range from 20° to 60°. The particle morphology was investigated via HR-TEM, TEM-FEI/PHILIPS CM120 microscopy. The surface composition of the nanoparticles was analyzed by X-ray photoelectron spectroscopy (XPS) measurements. A Scienta Omicron ESCA + spectrometer was used, consisting of a monochromatic source of Al Kα ($h\nu$ = 1486.7 eV) and a hemispherical analyzer (EA125). The spectra were corrected to the charge effects using the C 1s peak of adventitious carbon at 284.6 eV as a reference. All data analyses were made using CASA XPS software (Casa Software ltd., U.K.).

2.2. Fabrication of CeO_2 NR-based electrochemical immunosensor

The immunosensor consists of an electrochemical sensor board containing three integrated electrodes: a counter electrode (CE), a WE, and a reference electrode (RE), with the gold trails onto polymide which were purchased from PCBWAY Company. In the RE, a silver/silver chloride ink was deposited along with heat treatment at 60 °C. For the immunosensor WE fabrication, three conditions of deposition of the CeO_2 nanorods were tested on the WE in order to verify the best dispersion of the NRs and electrochemical response. Emulsions were made with 5 % m/m of polyvinylidene fluoride (PVDF) in CeO_2 NRs varying the emulsions with 50 % v/v Gluta (called CeO_2-Gluta), 50 % v/v DMF (called CeO_2-DMF). After these emulsions were prepared, they were added on the WE in the amount of 10 μL of emulsion on each electrode. The electrodes were then left for 18 h in a vacuum oven at 120 °C. A third condition was performed by repeating the CeO_2-DMF preparation procedure and inserting drops of a 10 % acetic acid solution on its surface, hydroxylating the surface, and called CeO_2-DMF hydroxylated (CDH).

2.3. Immobilization of the CRP

The anti-CRP antibody (ab50861, Abcam, Cambridge, UK) was immobilized via 20 mM Cystamine dihydrochoride (Cys, Alfa Aesar) and 2.5 % Glutaraldehyde (Glut) (Electron Microscopy Sciences) on the surface of CeO_2 NRs. The anti-CRP antibody was diluted in 0.1 M buffered phosphate saline (PBS) pH 7.4 at a concentration of 1:200, and a 25 μl volume of this antibody solution was dropped on the surface of the WE and incubated for 12 h at 4 °C. After incubation, the immunosensor was washed with PBS buffer to remove antibody excess.

2.4. Immobilization of the CRP and sample characterizations

Different concentrations (from 0.3 to 7 mg L^{-1}) of the CRP recombinant protein were incubated in the immunosensor at room temperature in a moist chamber, followed by washing with PBS buffer to remove antigen excess. Immunosensor performance was evaluated by calibration curve and limit of detection (LoD) by electrochemical measurements: cyclic voltammetry (CV) and differential pulse voltammetry (DPV). The Scheme 1 shows the details of the immunosensor preparation, the results that corroborate the functionalization steps are described in the next sections.

The measurements were performed using a portable potenciostat Sensit Smart connected to a notebook via PC software PSTrace. During the assays, the potential was scanned from −0.6 to 0.6 V at the scan rate of 100 mV s^{-1} and recorded in 10 mmol/L $K_4[Fe(CN)_6]$ and 0.5 mol/L with $NaNO_3$ solution as mediator. The samples were also characterized by Scanning Electron Microscopy (SEM) in an Inspect F50 SEM microscope and by Fourier Transform Infrared Spectroscopy (FTIR) analyses performed using a Thermo Scientic Smart iTR Nicolet iS10.

To test the specificity of CRP antibody-antigen binding, Dot Blot assays were performed. Recombinant Myoglobin, recombinant CRP, recombinant cardiac Troponin T (c-TnT) and recombinant cardiac Tro-

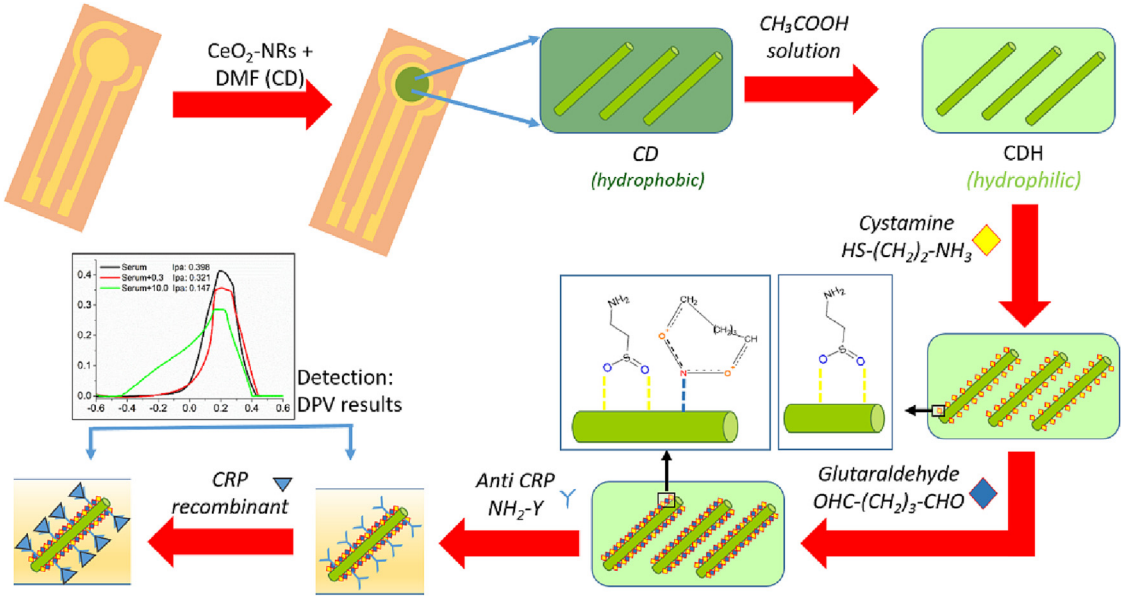

Scheme 1. Schematic illustration of the CDH immunosensor fabrication process for CRP determination.

ponin I (c-TnI) protein were characterized for dot blot analysis. 2 μL of samples were spotted with a pipette tip onto the nitrocellulose membrane at the center of the grid. The dots were made with 0.15 μg mL^{-1}, 0.015 μg mL^{-1}, and 1.5 ng mL^{-1}. The membranes were let to dry for 30 min and incubated overnight at 4 °C with a 1:500 mouse monoclonal anti-CRP antibody. The blots were subsequently washed in Tris-buffered saline solution with Tween and incubated with HRP conjugated secondary antibody. Immunoreactive bands were visualized with the enhanced chemiluminescence method.

The selectivity of the CRP immunosensor was verified using bovine fetal serum. The serum sample was spiked with CRP protein (10 mg mL^{-1} and 0.3 mg mL^{-1}), incubated for 60 min and characterized by CV analysis.

3. Results and discussion

3.1. Characterization of the bare board sensor and CeO_2 NRs on working electrode

The CeO_2 sample, used in WEs, showed a cubic crystal structure (ICSD pattern n° 239412), Fig. 1a. The morphology showed a smaller proportion of smaller particles, possibly nanocubes, and predominantly nanorods, with an average diameter of the rods of 12.0 nm, Fig. 1b. Fig. 1c and d show XPS analyses of the sample. In the survey spectrum, Fig. 1c, a material free of contamination is observed, presenting only Ce, O and C of adsorption. In order to characterize the chemical environment of Ce, the high resolution spectrum of Ce 3d is shown in Fig. 1d. The common presence of the mixture of the Ce^{4+} and Ce^{3+} oxidation states [37,38] is observed. The spin–orbit coupling of $3d_{5/2}$ and $3d_{3/2}$ are designated by v and u, respectively. The Ce^{3+} doubles are named u'/v' and u^0/v^0 referring to primary photoemission and its shakedown. The Ce^{4+} doubles are the u'"/v'" of the primary photoemission and u/v and u"/v" as their shakedown features.

The relative concentration of species with the Ce^{3+} oxidation state can be determined by the relative area of each component corresponding to the Ce^{3+} and Ce^{4+} oxidation states, using Eq. (1).

$$\%Ce^{3+} = \frac{AreaCe^{3+}}{(AreaCe^{3+} + AreaCe^{4+})} \times 100 \quad (1)$$

The results for the CeO_2 nanorods sample showed a concentration of Ce^{3+} at ~17 %. Works have shown that $Ce^{3+} \leftrightarrow Ce^{4+}$ reactions represent an effect of increasing the electrochemical activity of materials [39,40], which makes it an interesting possibility for applications as a biosensor, since such changes in oxidation state are related with variations in oxygen vacancies and interactions adsorption of biomolecules.

The WEs were then obtained using the CeO_2 nanorods and was evaluated the best deposition condition of the nanoparticles such as dispersion, porosity and adherence to the WE base. The electrodes used in this work are of the flexible type with CE configuration on the side, the WE in the center, and a silver/silver chloride layer on the gold trail for the RE, Fig. 2a. The deposition conditions of CeO_2 NRs were carried out by dispersing CeO_2 NRs in Gluta, CeO_2-Gluta (Fig. 2b and S1a) and DMF, CeO_2-DMF (Fig. 2c and S1b). Both deposition methodologies showed good deposition adhesion, however, the microscopic analyses show that the dispersion of CeO_2-Gluta presented a surface with greater porosity, more heterogeneity, and cracks compared to CeO_2-DMF.

Such factors are reflected in the results obtained in the voltammograms (Fig. 3a). For the bare board, CeO_2-Gluta and CeO_2-DMF electrodes, it is observed that the anodic peaks are located in the region of 0.2 V, which is to be expected in the presence of the $K_4[Fe(CN)_6]$. As for the anodic current density values, Ipa, there is a decrease presented by the electrodes in the following order: bare board > CeO_2-Gluta > CeO_2-DMF.

Due to the heterogeneous deposition characteristics of the CeO_2-Gluta electrode, the contact between the electrolyte and the bare board electrode results in a higher Ipa value compared to CeO_2-DMF. Despite the CeO_2-DMF electrode surface being more homogeneous, and the dispersing agent (DMF) presenting hydrophilic characteristics [41], the electrode surface was highly hydrophobic in electrochemical tests. This is due to the hydrophobic characteristic of the more stable surfaces of CeO_2 [42]. Thus, we to perform the hydroxylation of the CeO_2-DMF electrode surface with a 10 % aqueous solution of acetic acid, in order to make the electrode surface more hydrophilic. This electrode was then called CDH (CeO_2-DMF-hydroxylated) and is showed in the Fig. 2d. A greater surface disaggregation was observed with improved electrolyte adhesion during the experi-

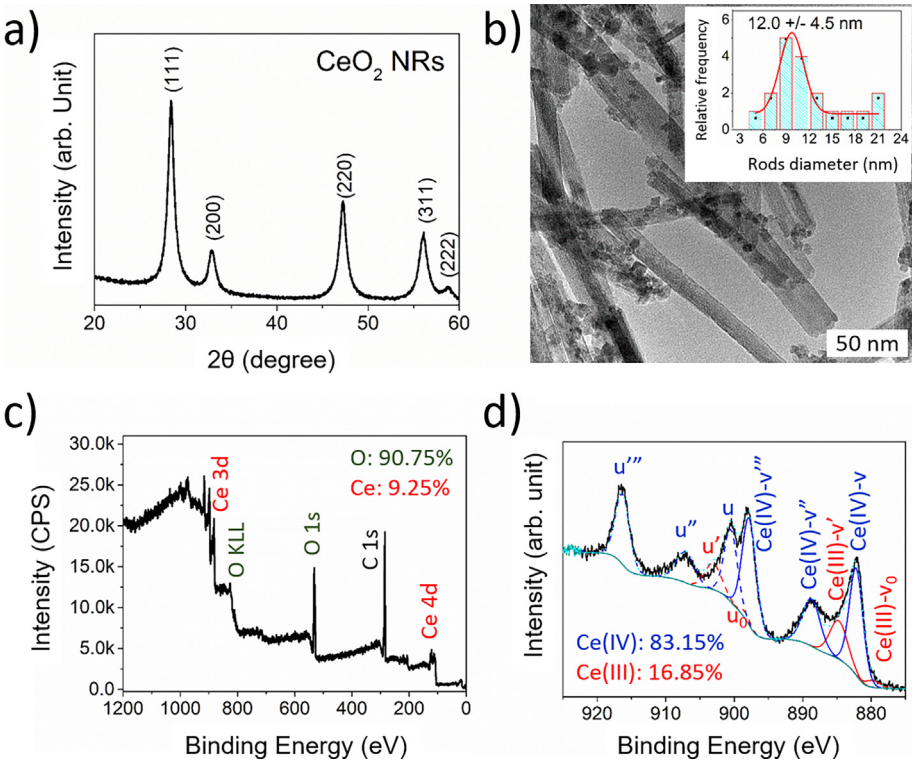

Fig. 1. Structural, morphological and surface composition results of the CeO_2 NRs, showing in a) the XRD, in b) the transmission electron microscopy image (inset: rod diameter distribution) and in c) and d) the XPS spectra referring to the survey and Ce 3d emission, respectively.

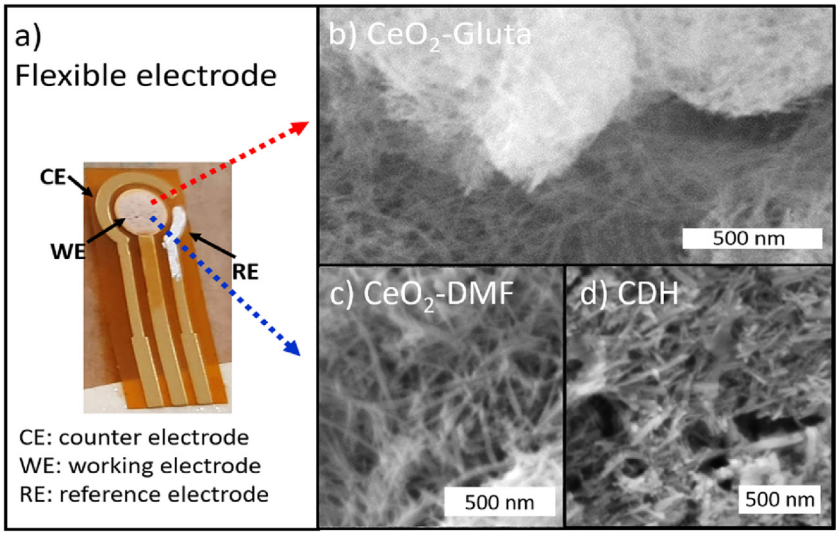

Fig. 2. Different deposition method analyses used in the preparation of WE. In (a) illustrates the flexible electrode used, in (b-d) SEM images for the electrodes: CeO_2-Gluta (b), CeO_2-DMF (c), and CeO_2-DMF hydroxylated, CDH (d).

ments. In order to calculate the active surface area of the electrodes, the Randles-Sevcik equation (Eq. 01) was used:

$$I_p = 2.69 \times 10^5 . n^{3/2} . A . D_0^{1/2} . [C] . v^{1/2} \quad (1)$$

Where I_p is the current maximum, n is the number of electrons transferred in the redox event, A is electrode area, D is diffusion coefficient of the $K_3[Fe(CN)_6]$ (7.6×10^{-6} cm^2 s^{-1}), [C] is concentration of the $K_3[Fe(CN)_6]$ (10 mM), and v is scan rate in 100 mV s^{-1}. The results showed that the CDH electrode has higher 35 % active surface area compared to before hydroxylation (CeO_2-DMF), indicating greater electron transfer and porosity in the material. The CDH electrochemical behavior resulted in changes in both Ipa and Epa compared to CeO_2-DMF. The current increase by 0.12 mA and the potential showed a shift of around 260 mV to a more positive potential compared to pre-hydroxylation. The increase to current is due to higher active surface and consequent reduced electrolyte/surface repulsion resulting in better mass transport and the increase in current density value.

In order to verify the reason for the potential shift observed for the CDH electrode, electrochemical analyzes were performed without the presence of the $K_3[Fe(CN)_6]$ solution, i.e., an analysis in the presence

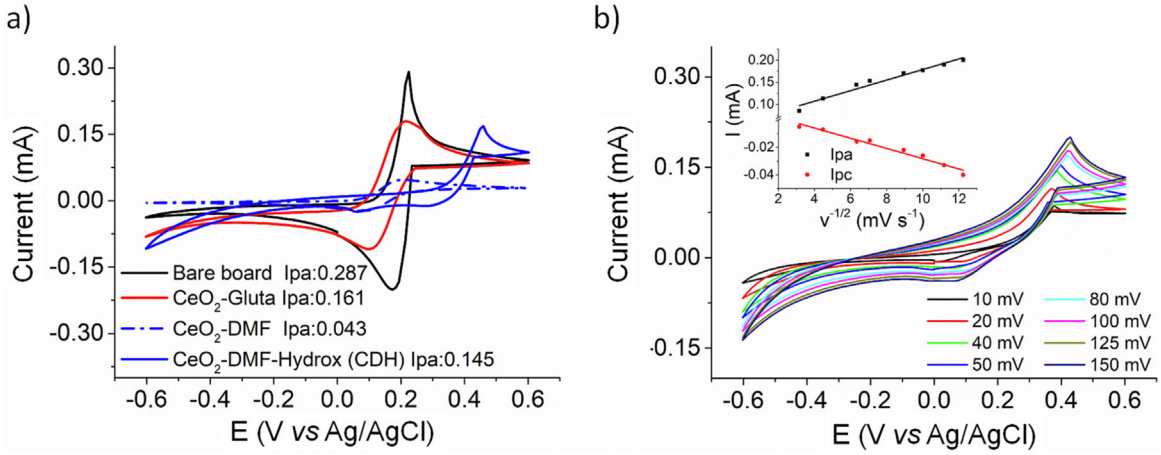

Fig. 3. CV curves to the bare board and the different CeO_2 depositions conditions (a) and scan rates to CDH (b). All the measurements were performed in the presence of $K_3[Fe(CN)_6]/K_4[Fe(CN)_6]$ (10 mM) in $NaNO_3$ (0.5 mol/L), with a scan rate of 100 mV s^{-1}.

only of the $NaNO_3$ electrolyte, voltammogram shown Fig. S2. In this case, the observed electrochemical behavior is directly related to the CeO_2 surface. In this voltammogram it is possible to observe two sharpest peaks, the anodic in the potential of the positive region (peak A_2, at 0.4 V) and the cathodic (peak C_1, at 0.0 V). There are also two less prominent changes in curve slope which indicate redox behavior observed in the anodic (peak A_1, at 0.10 V) and cathodic (peak C2, at −0.26 V) regions. As observed in the XPS analyses, the surface of CeO_2 is composed of a mixture of the valence states of Ce^{+3} and Ce^{+4}, with the Ce^{+4} species in greater proportion (87 %, Fig. 1d). Therefore, the sharpest anodic peak in the region of 0.4 V (peak A_2) is due to the oxidation of the species with the highest proportion on the surface, $Ce^{+3} \rightarrow Ce^{+4}$. While the anodic peak with the lowest evidence, peak A_1, is possibly related to the sum of the oxidation of the species with the lowest oxidation number ($Ce^{\pm}$, Ce^{+2}) for the Ce^{+3} species [43–45]. In turn, the C1 and C2 cathodic peaks correspond to the reduction reactions of the reactions demonstrated for the oxidation, that is, the species from Ce^{+4} to Ce^{+3} and from Ce^{+3} to species with a lower oxidation state, respectively. This results demonstrates that the cathodic potential shift towards more positive region observed at the CDH electrode is permanent even without the $[Fe(CN)_6]^{-3/-4}$ solution. Indicating that the hydroxylation of the electrode allows greater interaction of Ce^{+3} and Ce^{+4} species in the electrochemical behavior of the material, shifting the potential in the analysis.

Fig. 3b shows the CV curves for the CDH electrode subjected to different scan rates in order to study the electron diffusion of the CDH electrode. Voltamograms were recorded in the presence of $K_4[Fe(CN)_6]$ (10 mM) redox solution, in which is observed that the anodic and cathodic peaks exhibit a proportional and linear increase according to the scan rate. The Ipa and Ipc are directly proportional to the scan rate square root (inset of Fig. 2b) with the following linear regression equation: I_{pa} (mA) = 0.012 ν (V s^{-1}) + 0.0592 (r = 0.97) and I_{pc} = 0.0037 ν (V s^{-1}) + 0.009 (r = 0.97). It suggesting that the electrochemical behavior on electrode is a diffusion-controlled process [46].

3.2. CDH immobilization

Fig. 4a illustrates the absorption spectra in the infrared region for the CDH after immobilizations. The anti-C-reactive protein was immobilized via Cys, and Gluta, to obtain the immunosensor. The bands observed in the spectra for the CDH indicate vibrational modes referring to the NRs dispersing agent on the electrode, DMF [47]. The main changes in the spectrum observed after immobilization are: i) the vibrational mode located at 1660 cm^{-1} in the CDH referring to the C═O stretching of the DMF is shifted to 1710 cm^{-1} when it is on the surface of the functionalized CDH, ii) there is an increase in the intensity of the vibrational mode of stretching C—N located at 1493 cm^{-1}, iii) at 1590 and 1350 cm^{-1} there are bands referring to asymmetric and symmetrical N═O stretching vibrational modes, respectively, iv) at 1250 cm^{-1} the vibrational mode referring to the C—N asymmetric stretching is shifted to a higher wavenumber; and v) there are at 1220 and 1160 cm^{-1} related to C—O stretch vibrations. All these characteristics are related to the chemical interaction of Cys/Gluta-CRP antibody with the surface of the CDH electrode. It is observed that cystamine binds to the surface of the CDH primarily by covalent N—O bonds, verified mainly by the presence of the vibrational stretching modes in the functionalized CDH of the nitro groups (R-NOO, 1590 and 1350 cm^{-1}) and by the displacement of the band referring to the C═O stretch from 1650 cm^{-1} to 1710 cm^{-1} of DMF, indicating that the C═O group passes from an amide which before interacts with the NRs, with a weakened bond close to the scavenger electrons (N from DMF), and after immobilization, to a ketone with stronger vibration on the surface of the functionalized CDH. In this sense, the schematic illustration shown in Fig. 4b, indicates the mechanism of immobilization of Cystamine and glutaraldehyde on CDH dispersed in DMF. In the interaction, it is possible to observe that the oxygen and nitrogen groups adsorb on the nanorods, step (i), making the carbon of the amide group more positive and favoring the breakdown of the DMF molecule and the interaction of cystamine with the oxygens, step (ii). In next step, step (iii), there is the functionalization of glutaraldehyde, obtaining the respective functional groups observed by FTIR analysis, and indicating the exposure of the groups of Glutaraldehyde in order to favor the immobilization of the antibody.

Fig. 5a illustrates the CV curves for the CDH electrode and after its immobilizations. After immobilization with the anti-C-reactive protein antibody (CDH + Cys/Gluta + Im), named now as immunosensor, a 13 % reduction in the Ipa value is observed due to the insulating nature of the biomolecule [48], thus denoting the sensitivity of the immunosensor. The immunosensor reproducibility was verified with three different sensors (Fig. 5b), obtaining good reproducibility (coefficient of variation = 4.5 %), and then compared to the bare board (Fig. 5c). The stability of the immunosensor was assessed by ten successive CVs voltammograms (Fig. S3), with good repeatability (low variation of redox peaks: 9.6 % of coefficient of variation). Therefore, the low coefficient of variation values for both reproducibility and repeatability prove the quality of the immunosensor.

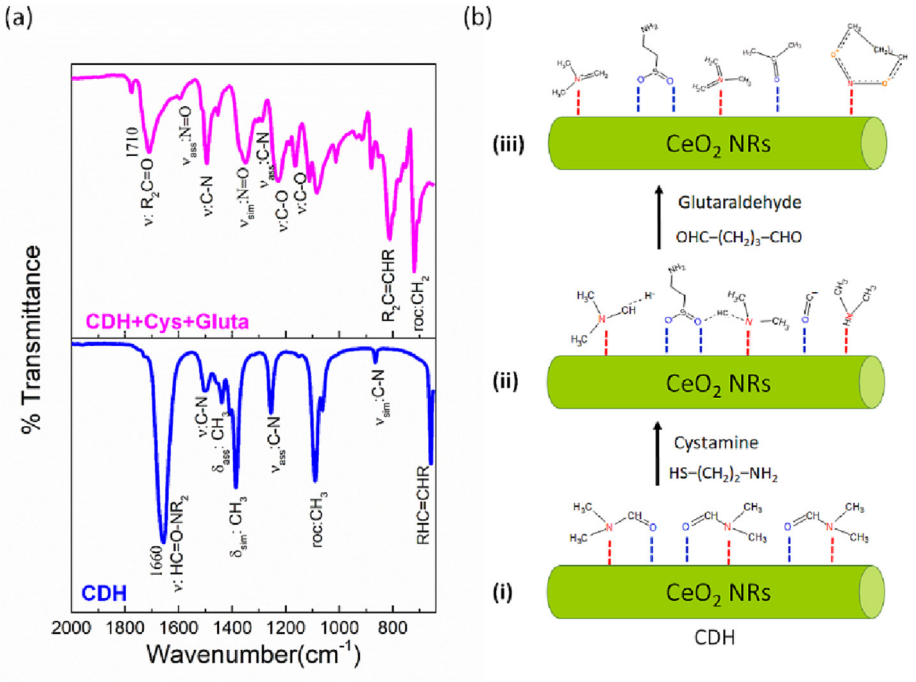

Fig. 4. Analyses for the obtained electrode (CDH) and immobilized, in (a) FTIR (ν, δ, roc, sim and ass are the symbols that denote stretching, deformation, rocking, symmetrical and asymmetrical, respectively), and (b) representative scheme of the interaction of cystamine and glutaraldehyde in nanorods of NRs CeO_2 dispersed in DMF.

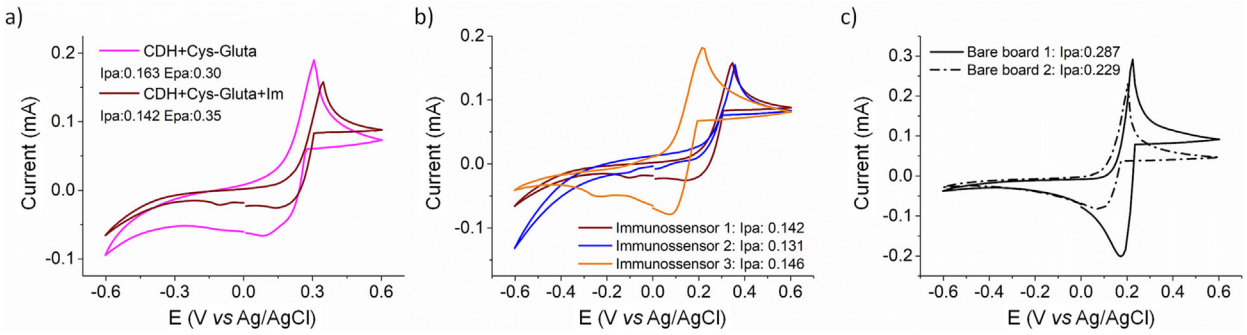

Fig. 5. CV curves (a) comparing the immobilization steps (b), the immunosensor reproducibility (b), and comparing the bare board reproducibility (c). All the electrochemical measurements were performed the presence of $K_3[Fe(CN)_6]/K_4[Fe(CN)_6]$ (10 mM) in $NaNO_3$ (0.5 mol/L), with a scan rate of 100 mV s^{-1}.

3.3. Immunosensor response to CRP

The electrodes were incubated with 20 μl of the different anti-CRP concentrations for 60 min at room temperature. The CRP concentrations chosen for the analyses were from 0.3 to 10.0 mg L^{-1} based on studies, which demonstrate that normal plasma CRP concentrations are below 1.0 mg L^{-1}, medium risk of 1.0–3.0 mg L^{-1}, and levels above 3.0 mg L^{-1} represent a high risk for cardiovascular disease [6,49,50]. The electrochemical results for the detection of CRP on the immobilized CDH electrode are shown in Fig. 6. Fig. 6a relates the intensity of CV measurements anodic peak as a function of the logarithm of the CRP concentration, the measurements were performed the presence of $K_3[Fe(CN)_6]$ (10 mM) in $NaNO_3$ (0.5 mol/L), with a scan rate of 100 mV s^{-1}. Comparing the detection of the lowest concentration of antigen CRP with the immobilized electrode (immunosensor, Fig. 4c), a reduction in the current density of the former is observed in relation to the second. The C-reactive protein antigen with a negative charge density when binding to immobilized CRP-antibody molecules (positively charged) decreases the sensor drainage current, thus reducing the current density values compared to the immunosensor, similar results were verified by other works [51,52]. As the concentration of CRP increases, there is an increase in the density of negative charge on the immunosensor, and consequently the current increases again. This is clearly observed when examining the different CRP concentrations by the DPV method, Fig. 6b, the peak current value is substantially increased as the CRP concentration increases.

It is observed, Fig. 6a, that for lower and higher concentrations there is a different behavior detection. For the first region (concentrations < 3.0 mg L^{-1}) data processing shows the linear regression equation as $I(mA) = 0.006$ [anti-CRP] + 0.1104 with $R^2 = 0.947$, and for the second region (concentrations > 3.0 mg L^{-1}) a linear regression as $I(mA) = 0.049$ [anti-CRP] + 0.1268 with $R^2 = 0.889$. These different detection regions found in the biosensor can be related with the threshold concentrations of antigen additions and access to the electrode surface [53]. The limit of detection, LOD, values found using the first and second linear regressions are 0.16 mg L^{-1} and 0.18 mg L^{-1}, respectively. This represents excellent detection results

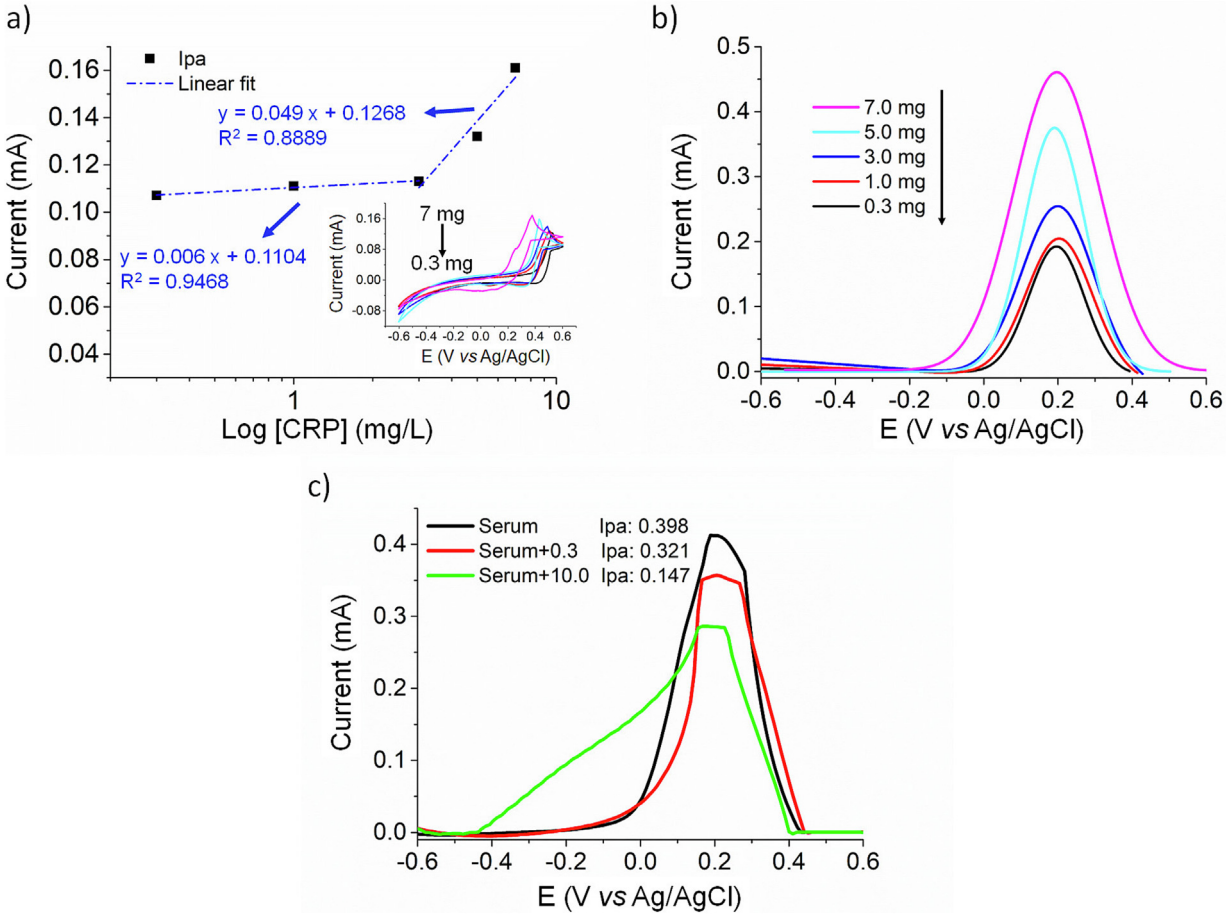

Fig. 6. (a) Response to linearity of calibration curve of the immunosensor to the anti-CRP (from 0.3 to 7.0 mg L^{-1}) obtained from the curved CVs (inset). (b) DPV for different concentrations of CRP. All the measurements were performed the presence of $K_3[Fe(CN)_6]/K_4[Fe(CN)_6]$ (10 mM) in $NaNO_3$ (0.5 mol/L), with a scan rate of 100 mV s^{-1}. (c) DPV to fetal bovine serum pure and with the presence of 0.3 and 10.0 mg L^{-1} of CRP.

for deregulated levels of CRP in the human body [54,55], and indicates that the LOD obtained allow measurements at clinical stages for the diagnosis of CRP alteration. The results obtained are also compared with recent research for the detection of CRP, Table 1, with the advantages of being a H_2O_2-free biosensor, easier to fabricate, being built on a portable flexible electrode, presenting a fast analysis time, and LOD within the levels for detection of dysregulated CRP.

In order to confirm the detection of antibody-antigen CRP, tests were performed in fetal bovine serum (FBS), preparing three samples, serum only immobilized with antibody without the presence of CRP antigen, and with 0.3 and 10.0 mg L^{-1} of CRP, the results are shown in Fig. 6c on DPV curves. The same electrochemical behavior is observed as in the ferrocyanide solution, there is a reduction in the Ipa value as CRP is added at low concentrations, however, for high

Table 1
Comparison of CDH-immunosensor LOD values with recent tests for the CRP diagnosis.

Method	Assay type	Immobilization and detection strategy	Sample type	Approximate analysis time (minute)	LOD (mg L^{-1})	Reference
CeO_2 Nanorods based electrochemical immunosensor	Flexible point-of care electrochemical biosensor	CeO_2 Nanorods modified by CRP antibody via cystamine and glutaraldheyde	Serum	0.5	0.18	This work
ELISA (enzyme-linked immunosorbent assays)	Microplate with bench absorbance spectroscopy	Used Dako polyclonal anti-CRP antibody for coating and Dako HRP-conjugated polyclonal anti-CRP antibody for detection besides commum Elisa reagents	Serum	~50	0.16	[56]
Nanoceria based lateral flow immunoassay	Point-of-care lateral flow immunoassay	Nanoceria@anti-CRP onto pre-treated conjugation nitrocellulose membrane	Serum	~15	0.12	[57]
Aptasensor based on ZIF67-Au	Bench electrochemical biosensor	AuNPs@C-ZIF67/GCE modified by aptamer via Au-thiol associated with CRP antibody labelled with HRP ($HRP\text{-}Ab_{CRP}$) with catalytic amplification using H_2O_2	Plasma	0.5	3.4×10^{-7}	[12]
PEI-Fc	Bench electrochemical biosensor	PEI-Fc onto CGE modified with antibody via free amino groups in the PEI-Fc structure	Plasma	0.5	2.5×10^{-3}	[17]

ZIF67-Au: rhomboid dodecahedra carbonized-ZIF67 loaded with gold nanoparticle modified by aptamer; PEI-Fc: Branched polyethylenimine functionalized with ferrocene residues; HRP: horse radish peroxidase; GCE: Glassy Carbon Electrode; HRP: horse radish peroxidase; H_2O_2: hydrogen peroxide.

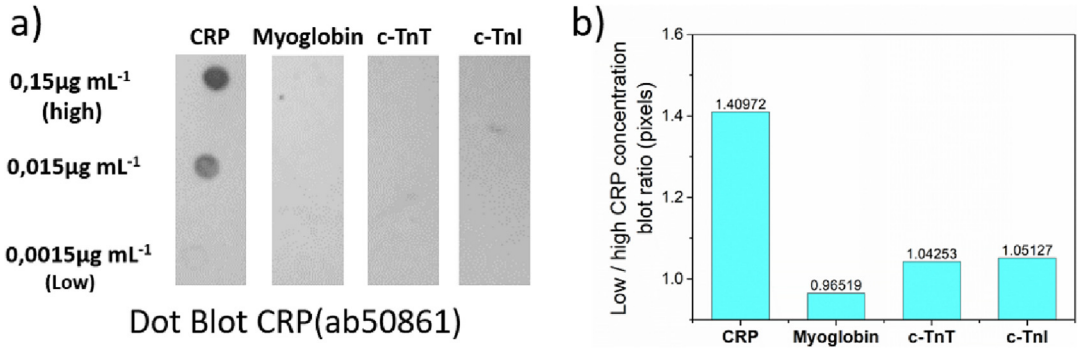

Fig. 7. (a) Specificity test, using dot blot, of the immunosensor for several CRP antigen concentrations and (b) intensity ratio in pixels between the highest and lowest CRP concentration.

concentrations of CRP (10.0 mg L^{-1}), the value of Ipa continues to decrease, different from the behavior observed in ferrocyanide. Peak current reduction can be considered by two main factors: i) the competitive adsorption between the analyte and the FBS or ii) the formation of a complex between the analyte and the FBS. Studies [58,59] on the interaction of FBS with different analytes, reveal a similar result reduction in Ipa, that is due to the formation of electroinactive complexes of the analyte with FBS, thus the concentration of free analyte is reduced, and consequently there is reduction in current value. Therefore, it is verified that the immunosensor allows the detection of CRP antigens in serum medium, which is compatible with clinical stage responses.

The antibody specificity used to build the immunosensor was evaluated by dot blot assay, Fig. 7a. This assay is a technique used in molecular biology to determine if the antibody or protein detection used is specific to the analyte. The most cardiac biomarkers in the blood are myoglobin, c-TnT and c-TnI. There is no blotting for the recombination of CRP antibodies with the myoglobin, c-TnT and c-TnI biomarkers, Fig. 7b, in which it is observed that the ratio between the blots of the lowest to the highest CRP concentration is approximately equal to 1, while for CRP this ratio is higher. The non-reactivity of the CRP antibody with these cardiac biomarkers demonstrates the specificity of the immunosensor. As the concentration of CRP increased, the color intensity ratio gradually increased, proving the immunosensor sensitivity, Fig. 7a-CRP.

4. Conclusion

An electrochemical immunosensor based on CeO_2 NRs was successfully obtained here for application as a rapid test for CRP detection. The CeO_2 NRs were dispersed in an organic agent and functionalized with cys and gluta which made them suitable for immobilization with the antigen–antibody CRP. The immunosensor showed good stability, sensitivity and reproducibility. In addition, the biosensor developed in this work is developed in a portable and flexible electrode, is free of oxidizing agents, does not have a high cost composition, few steps of synthesis and fast analysis time. Detection of the CRP immunosensor at above-normal levels was observed, making it an excellent candidate for applications as a portable biosensor for CRP. In the next stages of research, the validation of our immunosensor in human serum analysis is necessary.

CRediT authorship contribution statement

Amoresi Rafael Aparecido Ciola: Investigation, Conceptualization, Methodology, Writing - original draft, Writing - review & editing. **Roza Noemí Angelica Vieira:** Investigation, Methodology, Validation, Writing - review & editing. **Mazon Talita:** Investigation, Supervision, Resources, Writing – review & editing.

Declaration of Competing Interest

The authors declare that they have no known competing financial interests or personal relationships that could have appeared to influence the work reported in this paper.

Acknowledgments

The authors acknowledge the CEPID/CDMF, and the São Paulo Research Foundation (FAPESP), CEPID/CDMF (Proc. Nos. 2013/07296-2 and 2017/19143-7). The authors thank LME/LNNano – Brazilian Nanotechnology National Laboratory/CNPEM/MCTI by the support in SEM images. Research supported by CTI-Nano, strategic laboratory from SisNano, MCTI and financed by CNPq.

Appendix A. Supplementary data

Supplementary data to this article can be found online at https://doi.org/10.1016/j.jelechem.2023.117353.

References

[1] S.M. Nehring, B.C. Patel, C reactive protein (CRP), (2017).
[2] F.H. Epstein, C. Gabay, I. Kushner, Acute-phase proteins and other systemic responses to inflammation, N. Engl. J. Med. 340 (6) (1999) 448–454.
[3] S. Vanderschueren, D. Deeren, D.C. Knockaert, H. Bobbaers, X. Bossuyt, W. Peetermans, Extremely elevated C-reactive protein, Eur. J. Intern. Med. 17 (6) (2006) 430–433.
[4] G.M. Hirschfield, M.B. Pepys, C-reactive protein and cardiovascular disease: new insights from an old molecule, QJM 96 (2003) 793–807.
[5] T. Nagai, T. Anzai, H. Kaneko, Y. Mano, A. Anzai, Y. Maekawa, T. Takahashi, T. Meguro, T. Yoshikawa, K. Fukuda, C-reactive protein overexpression exacerbates pressure overload–induced cardiac remodeling through enhanced inflammatory response, Hypertension 57 (2) (2011) 208–215.
[6] B.M. Scirica, C.P. Cannon, M.S. Sabatine, P. Jarolim, S. Sloane, N. Rifai, E. Braunwald, D.A. Morrow, P.I. 22 Investigators, Concentrations of C-reactive protein and B-type natriuretic peptide 30 days after acute coronary syndromes independently predict hospitalization for heart failure and cardiovascular death, Clin. Chem. 55 (2009) 265–273.
[7] K.J.E. Sattler, J.E. Woodrum, O. Galili, M. Olson, S. Samee, F.B. Meyer, X.-Y. Zhu, L.O. Lerman, A. Lerman, Concurrent treatment with renin-angiotensin system blockers and acetylsalicylic acid reduces nuclear factor κB activation and C-reactive protein expression in human carotid artery plaques, Stroke 36 (1) (2005) 14–20.
[8] H. Sun, T. Koike, T. Ichikawa, K. Hatakeyama, M. Shiomi, B. Zhang, S. Kitajima, M. Morimoto, T. Watanabe, Y. Asada, C-reactive protein in atherosclerotic lesions: its origin and pathophysiological significance, Am. J. Pathol. 167 (2005) 1139–1148.
[9] H.-C. Kim, S.-K. Lee, W.B. Jeon, H.-K. Lyu, S.W. Lee, S.W. Jeong, Detection of C-reactive protein on a functional poly (thiophene) self-assembled monolayer using surface plasmon resonance, Ultramicroscopy 108 (10) (2008) 1379–1383.
[10] W. Gaede, Detection of classical swine fever with the LightCycler instrument, BIOCHEMICA-MANNHEIM-. (2002) 4–5.

[11] J.H. Lee, K.H. Yoon, K.S. Hwang, J. Park, S. Ahn, T.S. Kim, Label free novel electrical detection using micromachined PZT monolithic thin film cantilever for the detection of C-reactive protein, Biosens. Bioelectron. 20 (2) (2004) 269–275.

[12] S. Huang, Z. Liu, Y. Yan, J. Chen, R. Yang, Q. Huang, M. Jin, L. Shui, Triple signal-enhancing electrochemical aptasensor based on rhomboid dodecahedra carbonized-ZIF67 for ultrasensitive CRP detection, Biosens. Bioelectron. 207 (2022) 114129.

[13] S.K. Vashist, E.M. Schneider, J.H.T. Luong, Surface plasmon resonance-based immunoassay for human C-reactive protein, Analyst 140 (13) (2015) 4445–4452.

[14] W.M. Fakanya, I.E. Tothill, Detection of the inflammation biomarker C-reactive protein in serum samples: towards an optimal biosensor formula, Biosensors 4 (2014) 340–357.

[15] M.N.S. Karaboğa, M.K. Sezgintürk, Determination of C-reactive protein by PAMAM decorated ITO based disposable biosensing system: A new immunosensor design from an old molecule, Talanta 186 (2018) 162–168.

[16] Á. Molinero-Fernández, L. Arruza, M.Á. López, A. Escarpa, On-the-fly rapid immunoassay for neonatal sepsis diagnosis: C-reactive protein accurate determination using magnetic graphene-based micromotors, Biosens. Bioelectron. 158 (2020) 112156.

[17] A. Kowalczyk, J.P. Sęk, A. Kasprzak, M. Poplawska, I.P. Grudzinski, A.M. Nowicka, Occlusion phenomenon of redox probe by protein as a way of voltammetric detection of non-electroactive C-reactive protein, Biosens. Bioelectron. 117 (2018) 232–239, https://doi.org/10.1016/j.bios.2018.06.019.

[18] Y.-Y. Cheng, T. Zhan, X.-Z. Feng, G.-C. Han, A synergistic effect of gold nanoparticles and melamine with signal amplification for C-reactive protein sensing, J. Electroanal. Chem. 895 (2021) 115417.

[19] J.M. Pingarrón, P. Yáñez-Sedeño, S. Campuzano, New tools of Electrochemistry at the service of (bio)sensing: From rational designs to electrocatalytic mechanisms, J. Electroanal. Chem. 896 (2021) 115097.

[20] X. Luo, A. Morrin, A.J. Killard, M.R. Smyth, Application of nanoparticles in electrochemical sensors and biosensors, Electroanal. An Int. J. Devoted to Fundam. Pract. Asp. Electroanal. 18 (2006) 319–326.

[21] A. Gole, C. Dash, V. Ramakrishnan, S.R. Sainkar, A.B. Mandale, M. Rao, M. Sastry, Pepsin− gold colloid conjugates: preparation, characterization, and enzymatic activity, Langmuir 17 (2001) 1674–1679.

[22] A. Gole, S. Vyas, S. Phadtare, A. Lachke, M. Sastry, Studies on the formation of bioconjugates of endoglucanase with colloidal gold, Colloids Surfaces B Biointerfaces 25 (2) (2002) 129–138.

[23] R.M. Sambhaji, S. Warule, N.S. Chaudhari, B.B. Kale, K.R. Patil, P.M. Koinkar, M.A. More, Organization of cubic CeO2 nanoparticles on the edges of self assembled tapered ZnO nanorods via a template free one-pot synthesis: significant cathodoluminescence and field emission properties, J. Mater. Chem. 22 (2012) 8887–8895, https://doi.org/10.1039/c2jm30226h.

[24] J. Liu, M. Dai, T. Wang, P. Sun, X. Liang, G. Lu, K. Shimanoe, N. Yamazoe, Enhanced gas sensing properties of SnO2 hollow spheres decorated with CeO2 nanoparticles heterostructure composite materials, ACS Appl. Mater. Interfaces. 8 (2016) 6669–6677, https://doi.org/10.1021/acsami.6b00169.

[25] R.A.C. Amoresi, R.C. Oliveira, N.L. Marana, P.B. de Almeida, P.S. Prata, M.A. Zaghete, E. Longo, J.R. Sambrano, A.Z. Simões, CeO2 nanoparticle morphologies and their corresponding crystalline planes for the photocatalytic degradation of organic pollutants, ACS Appl. Nano Mater. 2 (10) (2019) 6513–6526.

[26] H.-X. Mai, L.-D. Sun, Y.-W. Zhang, R. Si, W. Feng, H.-P. Zhang, H.-C. Liu, C.-H. Yan, Shape-selective synthesis and oxygen storage behavior of ceria nanopolyhedra, nanorods, and nanocubes, J. Phys. Chem. B. 109 (51) (2005) 24380–24385.

[27] A.A. Ansari, A. Kaushik, P.R. Solanki, B.D. Malhotra, Sol–gel derived nanoporous cerium oxide film for application to cholesterol biosensor, Electrochem. Commun. 10 (9) (2008) 1246–1249.

[28] B. Zhu, P. Xia, W. Ho, J. Yu, Isoelectric point and adsorption activity of porous g-C3N4, Appl. Surf. Sci. 344 (2015) 188–195.

[29] M. Tsujimoto, K. Inoue, S. Nojima, Purification and characterization of human serum C-reactive protein, J. Biochem. 94 (1983) 1367–1373.

[30] Z. Bian, Y.M. Chan, Y. Yu, S. Kawi, Morphology dependence of catalytic properties of Ni/CeO2 for CO2 methanation: A kinetic and mechanism study, Catal. Today. 347 (2020) 31–38.

[31] B. Soni, S. Makkar, S. Biswas, Effects of surface structure and defect behavior on the magnetic, electrical, and photocatalytic properties of Gd-doped CeO2 nanoparticles synthesized by a simple chemical process, Mater. Charact. 174 (2021) 110990.

[32] H. Bi, L.-X. Zhang, Y. Xing, P. Zhang, J.-J. Chen, J. Yin, L.-J. Bie, Morphology-controlled synthesis of CeO2 nanocrystals and their facet-dependent gas sensing properties, Sensors Actuators B Chem. 330 (2021) 129374.

[33] R.A. Ciola Amoresi, R. Cristina de Oliveira, L. Cichetto, P.M. Desimone, C.M. Aldao, M.A. Ponce, L. Gracia, J.R. Sambrano, E. Longo, J. Andres, A.Z. Simões, Pure and Ni2O3-decorated CeO2 nanoparticles applied as CO gas sensor: experimental and theoretical insights, Ceram. Int. 48 (10) (2022) 14014–14025.

[34] Y. Xia, J. Lao, J. Ye, D.-G. Cheng, F. Chen, X. Zhan, Role of two-electron defects on the CeO2 surface in CO preferential oxidation over CuO/CeO2 catalysts, ACS Sustain. Chem. Eng. 7 (22) (2019) 18421–18433.

[35] X. Qian, Q. Qu, L. Li, X. Ran, L. Zuo, R. Huang, Q. Wang, Ultrasensitive electrochemical detection of Clostridium perfringens DNA based morphology-dependent DNA adsorption properties of CeO2 nanorods in dairy products, Sensors. 18 (2018) 1878.

[36] K. Dhara, D.R. Mahapatra, Review on electrochemical sensing strategies for C-reactive protein and cardiac troponin I detection, Microchem. J. 156 (2020), https://doi.org/10.1016/j.microc.2020.104857 104857.

[37] B.M. Reddy, A. Khan, Y. Yamada, T. Kobayashi, S. Loridant, J.-C. Volta, Surface characterization of CeO2/SiO2 and V2O5/CeO2/SiO2 catalysts by Raman, XPS, and other techniques, J. Phys. Chem. B 106 (42) (2002) 10964–10972.

[38] J.P. Holgado, R. Alvarez, G. Munuera, Study of CeO2 XPS spectra by factor analysis: reduction of CeO2, Appl. Surf. Sci. 161 (3-4) (2000) 301–315.

[39] S. Sonsupap, N. Chanlek, P. Kidkhunthod, T. Sinprachim, S. Maensiri, Synthesis and electrochemical properties of electrospun cerium oxide (CeO2) nanoparticles/carbon nanofibers, J. Electron. Mater. 51 (6) (2022) 2933–2948.

[40] X. Li, S. You, J. Du, Y. Dai, H. Chen, Z. Cai, N. Ren, J. Zou, ZIF-67-derived Co3O4@ carbon protected by oxygen-buffering CeO2 as an efficient catalyst for boosting oxygen reduction/evolution reactions, J. Mater. Chem. A 7 (45) (2019) 25853–25864.

[41] Z. Zhang, S. Xu, Y. Wu, S. Shi, G. Xiao, Recent advances of pervaporation separation in dmf/h2o solutions: A review, Membranes (Basel) 11 (2021) 455.

[42] M. Fronzi, M.H.N. Assadi, D.A.H. Hanaor, Theoretical insights into the hydrophobicity of low index CeO2 surfaces, Appl. Surf. Sci. 478 (2019) 68–74.

[43] H. Zhou, J. Xi, Z. Li, Z. Zhang, L. Yu, L. Liu, X. Qiu, L. Chen, CeO2 decorated graphite felt as a high-performance electrode for vanadium redox flow batteries, Rsc Adv. 4 (106) (2014) 61912–61918.

[44] B. Choi, J. Prabhuram, M.A. Scibioh, H.-I. Joh, Y.-E. Sung, H.Y. Ha, S.-K. Kim, High performance CeO2-And Ce0. 8Sm0. 2O2-modified Pt/C catalysts for the cathode of a DMFC, J. Electrochem. Soc. 156 (2009) B801.

[45] Z. Zhang, J. Liu, J. Gu, L. Su, L. Cheng, An overview of metal oxide materials as electrocatalysts and supports for polymer electrolyte fuel cells, Energy Environ. Sci. 7 (8) (2014) 2535–2558.

[46] J. Bard Allen, R. Faulkner Larry, Electrochemical methods: fundamentals and applications, (2001).

[47] M.M.E. Jacob, A.K. Arof, FTIR studies of DMF plasticized polyvinyledene fluoride based polymer electrolytes, Electrochim. Acta 45 (10) (2000) 1701–1706.

[48] A.M. Faria, T. Mazon, Early diagnosis of Zika infection using a ZnO nanostructures-based rapid electrochemical biosensor, Talanta 203 (2019) 153–160.

[49] T. Bryan, X. Luo, P.R. Bueno, J.J. Davis, An optimised electrochemical biosensor for the label-free detection of C-reactive protein in blood, Biosens. Bioelectron. 39 (1) (2013) 94–98.

[50] I. Kushner, D. Rzewnicki, D. Samols, What does minor elevation of C-reactive protein signify?, Am J. Med. 119 (2006) 166–e17.

[51] S. Noh, J. Kim, G. Kim, C. Park, H. Jang, M. Lee, T. Lee, Recent advances in CRP biosensor based on electrical, electrochemical and optical methods, Sensors 21 (2021) 3024.

[52] H.H. Lee, M. Bae, S.-H. Jo, J.-K. Shin, D.H. Son, C.-H. Won, H.-M. Jeong, J.-H. Lee, S.-W. Kang, AlGaN/GaN high electron mobility transistor-based biosensor for the detection of C-reactive protein, Sensors 15 (2015) 18416–18426.

[53] H.-J. Um, M. Kim, S.-H. Lee, J. Min, H. Kim, Y.-W. Choi, Y.-H. Kim, Electrochemically oriented immobilization of antibody on poly-(2-cyano-ethylpyrrole)-coated gold electrode using a cyclic voltammetry, Talanta 84 (2) (2011) 330–334.

[54] A.T.E. Vilian, W. Kim, B. Park, S.Y. Oh, T. Kim, Y.S. Huh, C.K. Hwangbo, Y.-K. Han, Efficient electron-mediated electrochemical biosensor of gold wire for the rapid detection of C-reactive protein: A predictive strategy for heart failure, Biosens. Bioelectron. 142 (2019) 111549.

[55] M.N. Sonuç Karaboga, M.K. Sezginturk, Determination of C-reactive protein by PAMAM decorated ITO based disposable biosensing system: A new immunosensor design from an old molecule, Talanta 186 (2018) 162–168, https://doi.org/10.1016/j.talanta.2018.04.051.

[56] T.L. Wu, K.C. Tsao, C.P.Y. Chang, C.N. Li, C.F. Sun, J.T. Wu, Development of ELISA on microplate for serum C-reactive protein and establishment of age-dependent normal reference range, Clin. Chim. Acta 322 (2002) 163–168, https://doi.org/10.1016/S0009-8981(02)00172-9.

[57] D.Y. Kong, N.S. Heo, J.W. Kang, J.B. Lee, H.J. Kim, M.I. Kim, Nanoceria-based lateral flow immunoassay for hydrogen peroxide-free colorimetric biosensing for C-reactive protein, Anal. Bioanal. Chem. 414 (10) (2022) 3257–3265.

[58] L. Fotouhi, S. Banafsheh, M.M. Heravi, Electrochemistry of the interaction of furazolidone and bovine serum albumin, Bioelectrochemistry 77 (1) (2009) 26–30.

[59] Y. Wu, X. Ji, S. Hu, Studies on electrochemical oxidation of azithromycin and its interaction with bovine serum albumin, Bioelectrochemistry 64 (1) (2004) 91–97.